A Global Spectral Model with a Finite Element Formulation for the Vertical Discretization: Adiabatic Formulation

MICHEL BÉLAND AND CHRISTIANE BEAUDOIN

Division de recherche en prévision numérique, Dorval, Québec, Canada H9P 1J3

(Manuscript received 21 November 1984, in final form 30 May 1985)

ABSTRACT

A finite element formulation for the vertical discretization of a global spectral model is presented. Results obtained from a linearized version of the model are compared with both exact analytical solutions and those of a vertically staggered finite-difference scheme. A series of seven-day global integrations using the fully nonlinear model and simple physics is presented and compared with the corresponding series obtained using a vertically staggered finite-difference model. The finite-element version of the model seems to give better performance, particularly at medium range. The new formulation tested here is also shown to be free of a noise problem present in an older version of the model.

1. Introduction

Some years ago, work was started at RPN (Recherche en prévision numérique) on the formulation of a fully Galerkin tri-dimensional model. The spectral method, with spherical surface harmonics as basis functions, was used in the horizontal, and a Galerkin finite element method was used in the vertical, with piecewise linear (Chapeau) functions. The results of a limited number of short term hemispheric integrations were presented and discussed in Staniforth and Daley (1977, hereafter referred to as SD77). A qualitative assessment of the 36-hour forecasts was positive. However, as length of the forecast period was increased and a more thorough quantitative assessment made, two problems were detected.

The first was related to treatment of the upper boundary condition. Since the vertical discretization was nonstaggered, and the top of the atmosphere extended to $\sigma = 0$ (where $\sigma = p/p_s$, p is pressure and p_s the surface pressure), SD77 had to face the awkward problem of defining values of the prognostic variables at $\sigma = 0$. In effect, they solved that problem by introducing additional *ad hoc* assumptions about the atmosphere as $\sigma \rightarrow 0$. It turned out that when these assumptions were relaxed (i.e., putting a finite top at $\sigma \neq 0$) some integrations showed improvement, as shown for example in Beaudoin and Staniforth, 1980.

The second problem was the appearance, as length of the forecast increased, of a two grid-length vertical computational mode. It was shown in Béland *et al.* (1982) that an *ad hoc* vertical diffusion term would very efficiently control this vertical uncoupling. Yet it was not until very recently that the cause of the problem was identified. This ultimately lead to the following formulation which appears to be free of these two shortcomings.

Section 2 presents a brief description of the model, stressing two important differences with Daley *et al.* (1976, hereafter referred to as D76) and SD77; Section 3 discusses the application of the finite element method to the model equations, and Section 4 presents the results of a set of linear and nonlinear integrations (the latter with global FGGE data), with emphasis on the accuracy of the method. Conclusions are given in Section 5.

2. The model

Derivation of the model equations is mostly standard and only differs in detail from D76 and SD77. Following a reviewer's comment, we refer the reader to these two publications for definitions of the symbols and variables used in this section, and for a more detailed description of the application of the spectral method and the semi-implicit time discretization scheme to the predictive equations that result. In what follows, we will simply point out the two important differences between this model and the models described in D76 and SD77, and how these differences modify the application of the finite element method originally described in SD77.

The first difference is the imposition of the top boundary condition $\dot{\sigma} = 0$ at $\sigma = \sigma_1 \neq 0$ (where subscript "1" denotes the top sigma-level of the model). We recall that in SD77, the authors were forced to assume the existence of an isothermal motionless atmosphere in the top layer in order to be able to close the problem. This arbitrary assumption also complicated the model code in that two different expansion domains had to be carried, one extending from $\sigma_0 = 0$ for the variable W, the other extending from $\sigma_1 \neq 0$ for all the other variables. This change results in a redefinition of the caret operator as follows:

$$(\hat{\ }) = \frac{1}{1-\sigma_1}\int_{\sigma_1}^{1}(\ )d\sigma. \tag{2.1}$$

Using Eq. (2.7) of SD77 with the new definition (2.1), the top boundary condition on W is now written

$$W(\sigma_1) = \sigma_1 W(1). \tag{2.2}$$

We note that in the limit $\sigma_1 \to 0$, we recover the formulation of SD77, as given in their Eqs. (3.14)–(3.18). A version of the model described in SD77 was accordingly coded taking into account the changes implied by (2.1) and (2.2). We shall refer to this version as model M2 in Section 4.

The second difference in some sense follows logically from the first one. Use of the semi-implicit method of Robert *et al.* (1972) usually leads to a coupled system of three integro–differential equations for the unknown variables D^+, T^+, and q^+, where a superscript "+" indicates a value of the variable at $t + \Delta t$. An efficient way to solve this system is to form a second-order differential equation (in σ) in one unknown for either the variable P^+ (method 1) or the variable W^+ (method 2), where

$$P = \phi + RT^*q, \tag{2.3}$$

$$W = \hat{D}^{\sigma} - \hat{D}. \tag{2.4}$$

In D76 (where a second-order staggered vertical finite difference scheme is used), method 1 was chosen, which led to their Eq. (53). In SD77, method 2 was chosen, which led to their Eq. (3.14). It turns out that method 2 can also be applied, with identical results, to the model of D76 (it is in fact a version of this model that is currently in use at the Canadian Meteorological Center and which we call model M3 in Section 4). However, the converse is not true: method 1 cannot be used with the model of SD77. The reason for this was pointed out in SD77, and is related to the mapping of geopotential to σ which is singular at $\sigma = 0$. Now by applying the top boundary condition (2.2) at $\sigma_1 \neq 0$, this singularity formally disappears, and method 1 can be implemented without any problems in the model of SD77 (we shall comment in Section 4 as to why one would like to do so). Thus, Eq. (3.14) of SD77 can be replaced by Eq. (53) of D76.

However, the same approach [*viz.* replacing Eq. (3.15) of SD77 by Eqs. (61) and (63) of D76] cannot be used for the boundary conditions. Because of the staggering used in D76, *ad hoc* assumptions had to be made for the values of the static stability $\tilde{\gamma}_N$ and the vertical velocity $\dot{\tilde{\sigma}}_N$ near the surface $\sigma_N = 1$, these values being needed in the derivation of their surface boundary condition Eq. (63). The particular form of the finite element method used in SD77 is nonstaggered, and all the predictive variables are defined on the same levels, up to and including the $\sigma_N = 1$ level. Hence no assumptions are needed in the derivation of the boundary conditions. We shall now sketch this derivation for clarity.

We first take $\partial/\partial t$ of (2.3):

$$\frac{\partial P}{\partial t} = \frac{\partial \phi}{\partial t} + RT^*\frac{\partial q}{\partial t}. \tag{2.5}$$

We then take $\partial/\partial\sigma$ of (2.5), and use the hydrostatic equation to substitute for $\partial\phi/\partial\sigma$:

$$\frac{\partial}{\partial t}\left(\frac{\partial P}{\partial \sigma}\right) = -\frac{R}{\sigma}\frac{\partial T'}{\partial t} + R\frac{dT^*}{d\sigma}\frac{\partial q}{\partial t}.$$

After multiplying through by σ/R, we get

$$\frac{\partial}{\partial t}\left[\frac{\sigma}{R}\frac{\partial P}{\partial \sigma}\right] = -\left[\frac{\partial T'}{\partial t} - \sigma\frac{dT^*}{d\sigma}\frac{\partial q}{\partial t}\right]. \tag{2.6}$$

We may substitute directly from the thermodynamic equation [in the form given in Eq. (3.3) of SD77] for the rhs of (2.6); rearranging terms, we get:

$$\frac{\partial}{\partial t}\left[\frac{\sigma}{R}\frac{\partial P}{\partial \sigma}\right] + \gamma^* W = -J, \tag{2.7}$$

where W is defined in (2.4) and J is defined in SD77. Equation (2.7) is now applied at the top boundary $\sigma = \sigma_1$ and the surface boundary $\sigma_N = 1$.

At the surface $\sigma_N = 1$, we use the continuity equation (3.4) of SD77 to express W_s (where a subscript "s" denotes a value of the variable at $\sigma_N = 1$) in terms of $\partial q/\partial t$:

$$\frac{\partial q}{\partial t} = W_s - \hat{\mathbf{V}}\cdot\nabla q. \tag{2.8}$$

Moreover, since ϕ_s is time-invariant, we obtain another equation relating q and P at the surface from (2.5) evaluated at $\sigma_N = 1$:

$$\frac{\partial q}{\partial t} = \frac{1}{RT_s^*}\frac{\partial P_s}{\partial t}. \tag{2.9}$$

Equating (2.8) and (2.9), and substituting from W_s in (2.7) evaluated at $\sigma_N = 1$ finally yields the surface boundary condition on P:

$$\frac{\partial}{\partial t}\left[\left(\frac{\sigma}{\gamma^* R}\right)\frac{\partial P}{\partial \sigma} + \frac{\sigma}{RT_s^*}P_s\right]\Bigg|_{\sigma=1} = \left[-\hat{\mathbf{V}}\cdot\nabla q + \frac{J}{\gamma^*}\right]\Bigg|_{\sigma=1}. \tag{2.10}$$

At the top of the model atmosphere $\sigma = \sigma_1$, we substitute in (2.7) for $W(\sigma_1)$ using (2.2), and then proceed as above. The resulting equation is formally identical to (2.10) except for the fact that it is evaluated at $\sigma = \sigma_1$. These two boundary conditions are sufficient to close the system [note that both have made use of the original boundary condition $\dot{\sigma} = 0$ at $\sigma = (1, \sigma_1)$ which is implicit in the continuity equation (2.8)].

Summing up the differences with SD77, Eqs. (3.14) and (3.15) of SD77 are replaced, in their time-discretized version, by

$$\langle P^+\rangle_{\sigma\sigma} + (\Delta t^2\nabla^2)P^+ = L, \tag{2.11}$$

$$\langle P^+\rangle_\sigma + \left(\frac{\sigma}{RT_s^*}\right)P_s^+ = M, \quad \text{at} \quad \sigma = \sigma_1 \quad \text{or} \quad \sigma = 1, \tag{2.12}$$

where $\langle\ \rangle_\sigma = \frac{\sigma}{R\gamma^*}\frac{\partial}{\partial\sigma}$, and $\langle\ \rangle_{\sigma\sigma} = \frac{\partial}{\partial\sigma}\langle\ \rangle_\sigma$, and where

$$K = (-\Delta t^2\Delta^2)P^- + D^- + 2\Delta t[\alpha(B, -A) - a^2\nabla^2 E],$$

$$L = \langle P^-\rangle_{\sigma\sigma} + \Delta t D^- + \Delta t K + 2\Delta t\left\{G + \frac{\partial}{\partial\sigma}\left[\frac{1}{\gamma^*}(\alpha(UT', VT') - B_T)\right]\right\},$$

$$M = \langle P^-\rangle_\sigma + \left(\frac{\sigma}{RT_s^*}\right)P_s^- + \frac{2\Delta t}{\gamma^*}[\alpha(UT', VT') - B_T],$$

all other symbols and/or variables being as originally defined in D76. Furthermore, Eq. (3.16) of SD77 is eliminated, since it is implicitly contained in (2.11) via (2.9), Eq. (3.17) of SD77 is replaced by

$$D^+ + (\Delta t\nabla^2)P^+ = K,$$

and finally Eq. (3.18) of SD77 remains as is. Otherwise, the solution procedure is identical. We will refer to this model as model M1 in Section 4.

3. Vertical discretization

Except for the fact that a single expansion domain is now used, the application of the finite element method to M1 follows closely SD77; we also refer the reader to Côté *et al.* (1983, herafter denoted C83) for a detailed description of the method. The definition of the basis function $e^k(\sigma)$ is also given in Appendix A of this paper, along with some definitions of operators. Here, we will content ourselves with a detailed description of the solution of (2.11)–(2.12).

After multiplying the lhs of (2.11) by $e^k(\sigma)$, and integrating the first term by parts, we obtain, for a given value of k:

$$\langle P^+\rangle_\sigma e^k|_{\sigma_1}^{\sigma_N} - \int_{\sigma_1}^{\sigma_N}\langle P^+\rangle_\sigma\frac{de^k}{d\sigma}\,d\sigma + (\Delta t^2\nabla^2)\int_{\sigma_1}^{\sigma_N}P^+e^k d\sigma; \tag{3.1}$$

the first term of (3.1) is obtained from the boundary conditions (2.12) by direct substitution. For the second term, we make use of our (relative) freedom in the choice of γ^* (see C83) and write $\gamma^* = \gamma_0\sigma^\alpha$; as an example, if a constant reference temperature T^*, say 300 K, is chosen for the semi-implicit scheme, we get $\alpha = -1$, $\gamma_0 = RT^*/c_p$. Thus, after expanding P^+ the second and third term may be written

$$\sum_{i=1}^{N}P_i^+\left\{-\frac{1}{R\gamma_0}\int_{\sigma_1}^{\sigma_N}\sigma^{1-\alpha}e_\sigma^i e_\sigma^k d\sigma + (\Delta t^2\nabla^2)\int_{\sigma_1}^{\sigma_N}e^i e^k d\sigma\right\}, \quad \forall\ k\in[1, N], \tag{3.2}$$

where a subscript σ means differentiation by this variable. The integrals appearing in (3.2) lead to the definition of two $N\times N$ tridiagonal matrices, which we represent, in operator notation, by $\mathbf{P}_{\sigma\sigma}^\beta$ and $\mathbf{P}$, namely the second derivative operator with respect to sigma (weighted by σ^β) and the projection operator (see Appendix A for their definition). The value $\mathbf{P}_{\sigma\sigma}^\beta$ is really quasi-tridiagonal since it contains the boundary condition [i.e., first term of (3.1)]. Letting $\mathbf{P}^+(\mathbf{P}^-)$ designate a column vector of length N, we may write (3.1) in more compact form as

$$\{\mathbf{P}_{\sigma\sigma}^\beta + (\Delta t^2\nabla^2)\mathbf{P}\}\mathbf{P}^+, \quad \beta = 1 - \alpha. \tag{3.3}$$

Once the rhs of (2.11) is computed, $\mathbf{P}^+$ is obtained by a Gaussian elimination technique. The matrices are time-independent and computed only once at the beginning of the forecast, and the elimination step (for the lhs matrices) is performed once and for all (one matrix per horizontal eigenvalue of ∇^2 is needed). Thus the solution scheme is quite efficient.

For the rhs, we use essentially the same procedure of integrating by parts the $\langle P^-\rangle_{\sigma\sigma}$ term and the $\partial/\partial\sigma$ term, using again the boundary conditions (2.12). We thus get an exact cancellation of M, and the rhs of (2.11) takes the form

$$\{\mathbf{P}_{\sigma\sigma}^\beta\}\mathbf{P}^- + \int_{\sigma_1}^{\sigma_N}\Delta t(D^- + K + 2G)e^k d\sigma - \frac{2\Delta t}{\gamma_0}\int_{\sigma_1}^{\sigma_N}\sigma^{-\alpha}[\alpha(UT', VT') - B_T]e_\sigma^k d\sigma. \tag{3.4}$$

After expanding the dependent variables in finite-element space, we again end up with a series of products of tridiagonal matrices times column vectors of known quantities. At this point, the method resembles qualitatively a finite-difference method, the only difference being that the weights by which the dependent variables are multiplied have been chosen by a Galerkin procedure. Thus, for example, products such as UT', VT' are performed without any aliasing in the vertical (with respect to the finite-element space chosen), as well as in the horizontal, since at this stage, we are on the Gaussian grid.

We now discuss the solution of two other equations, namely the hydrostatic equation and the diagnostic equation for $\dot\sigma$ [Eq. (20) of D76], which can be viewed as a form of the continuity equation (2.8). These two equations may both be put in a very similar form (that of a first-order partial differential equation) by defining $f(\sigma) = \hat D^\sigma + \hat G^\sigma$, where by definition, $f(1) = f_s = 0$. Then, solving for either Φ' or $\dot\sigma$ requires the solution of the following problem,

$$\frac{\partial f}{\partial\sigma} = \sigma^\beta g(\sigma), \quad f(1) = f_s \quad \text{given}, \tag{3.5}$$

where $g(\sigma) = -RT'$, $\beta = -1$ for the hydrostatic equation, and $g(\sigma) = -D - G$, $\beta = 0$ for the "continuity equation" [in the last case, $\dot\sigma$ is obtained from $f(\sigma)$ by

the relation

$$\dot{\sigma} = f + \frac{(\sigma - 1)}{(1 - \sigma_1)} f(\sigma_1) \Big].$$

At this point, the problem can be solved in the Galerkin framework by multiplying both sides by the basis functions $e^k(\sigma)$, $\forall\ k \in [1, N]$, integrating from σ_1 to σ_N, substituting the boundary condition

$$f_s = \begin{Bmatrix} \Phi'_s \\ 0 \end{Bmatrix}$$

for the last line of the resulting matrices, and using Gaussian elimination to solve for $f(\sigma)$ (again, the elimination step can be done once and for all since the coefficients are constants in time). In the case of N equally spaced σ levels, this algorithm yields second-order accuracy in the interior points, and first-order accuracy at the end points for $\beta \neq 0$. However, recognizing that in the near future the levels will be unequally spaced, one of us (J. Côté from RPN) has devised a scheme which, for the same computational effort, yields fourth-order accuracy at all points for the solution of (3.5) at unequally spaced levels. This scheme is described in Appendix B and is used in the present model for Φ' (and will shortly be used also for $\dot{\sigma}$).

4. Results

a. *Linear integrations*

In B83 and C83, results were presented with an earlier version of the model described above. Although the results were judged satisfactory when compared with an equivalent staggered finite-difference scheme, the experiments revealed two shortcomings: the first was a slowing down of the gravity modes much larger than that associated with the companion staggered finite-difference scheme, and the second was the presence of a two grid-length vertical computational mode. This last problem was particularly evident when a friction term was included, but it was still present in frictionless simulations (for example, see Fig. 4a of B83). In C83, the cause of the slowing down was identified [see Eq. (10.19) and (10.20) of C83]: the $W_{\sigma\sigma}$ term appearing on the left-hand (implicit) side is not handled the same way as in the right-hand (explicit) side. This can be stated explicitly by the inequality

$$\mathbf{P}_{\sigma\sigma} \neq (\mathbf{P}_\sigma - \Delta)\mathbf{P}^{-1}\mathbf{P}_\sigma, \qquad (4.1)$$

where $\mathbf{P}_{\sigma\sigma}$, $\mathbf{P}_\sigma$, $\mathbf{P}^{-1}$ and Δ are respectively the second and first derivative operator, the inverse projection operator and the "Kronecker delta" operator, all defined in C83. In other words, the eigenvalues of $\mathbf{P}_{\sigma\sigma}^{-1}$ times the right-hand side of (4.1) lie between 0^+ and 1, thus effectively reducing the value of the Coriolis term which it multiplies, and consequently reducing the computational gravity wave frequencies. This in itself would not be of great consequence in a global forecast model, since the semi-implicit scheme also slows down gravity waves, so that they are not treated accurately in any case.

There is however a much more negative consequence of the inequality (4.1): the inverse projection operator $\mathbf{P}^{-1}$ mixes together values from the N σ-levels of the model, thus effectively raising the order of the difference equation (10.19) of C83 to N, whereas the original analytical equation is of order 2 in σ. The result is the generation of an ensemble of computational modes along with an approximation to the analytical solution (the so-called physical mode). One of these modes is the two grid-length vertical computational mode which, although stable, is eventually excited by numerical noise and shows up as a vertical uncoupling of the solution. Now it so happens that in the new formulation presented in Sections 2 and 3, which leads to Model M1, Eqs. (3.3) and (3.4), which are the nonlinear difference equations equivalent to Eq. (10.19) of C83, do not contain an inequality of the form (4.1), and in particular should neither slow down the gravity modes, nor generate vertical computational modes. In order to verify this, we have rerun the experiments described in B83, but using a linear version of the new version described above. In fact, this linear version possesses the same set of analytical eigenmodes and eigenvalues as in B83, except that now, instead of solving for W^+ as in B83, we form an equation for P^+ (2.11), using the same basic state atmosphere as in B83, and the same linearization procedure. Two cases will be presented; the external Rossby mode and the third internal gravity mode. We refer the reader to B83 for a more detailed account of the procedure.

We have plotted in Fig. 1 the vertical profiles of the vorticity associated with the external Rossby mode, at initial time (curve on the left), and after a 500 time-step integration covering exactly 10 periods (629.9 hours) of the analytical solution (curves on the right). The continuous line is the exact solution, while the coarse dashed line is a staggered finite difference (FD) scheme similar to the one presently used in the Canadian Meteorological Center's operational spectral model (it is identical to the scheme described in B83, except that the geometric averaging for the 10 staggered σ-levels has now been replaced by an arithmetic averaging, thereby eliminating the spurious behavior near the top of the model atmosphere which was depicted in B83). The fine dashed line corresponds to the old finite element version, and the slightly coarser dashed line corresponds to the new version. One observes that the two grid-length wave has now been eliminated completely, as expected. The three numerical solutions still lag the exact solution, this lag being caused by the slowing down effect of the semi-implicit scheme. The lag is slightly less for the FD scheme, because its vertical truncation error is such as to overestimate the phase speed, thereby cancelling slightly the underestimate related to the semi-implicit scheme.

Figure 2 contains similar plots for the third internal

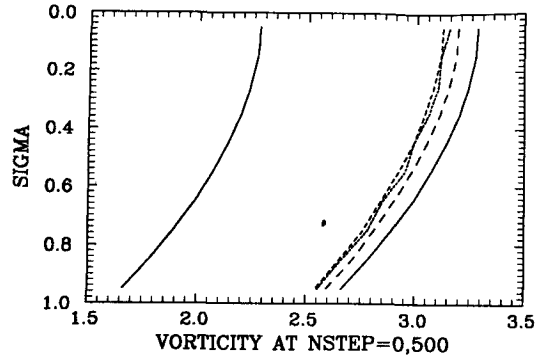

FIG. 1. Vertical profiles of vorticity (scaled by 10^5 s^{-1}) at initial time (left) and after a 500 time-step integration (right) covering exactly 10 periods of the exact external Rossby mode solution. Full line is the exact solution; small dashed line is the old finite-element version, medium dashed line is the new finite-element version, and coarse dashed line is a staggered finite difference version.

gravity mode. We now observe the complete elimination of the spurious slowing down of the gravity mode. Moreover, the finite element solution is now clearly seen to be more accurate than the FD solution: the amplitudes of the maximum and minimum are almost preserved exactly, while there is a relatively pronounced smoothing effect produced by the FD scheme. In fact, there are actually 5 curves on the right of Fig. 2! As mentioned in Section 4, it is possible to devise a fully fourth-order scheme which is as efficient as the standard finite element technique described earlier. This scheme is described in Appendix B; after 500 time steps, its accuracy is such that the curve depicting the numerical solution is indistinguishable from the exact solution, up to the first three significant digits.

b. *Nonlinear integrations*

The three models described in Section 2 as M1, M2 and M3 were used for these integrations. Table 1 summarizes the differences between them. Both models 1 and 2 (hereafter denoted M1 and M2) are finite-element models, the first one formulated to solve a Helmholtz equation for P^+, the second one formulated to solve

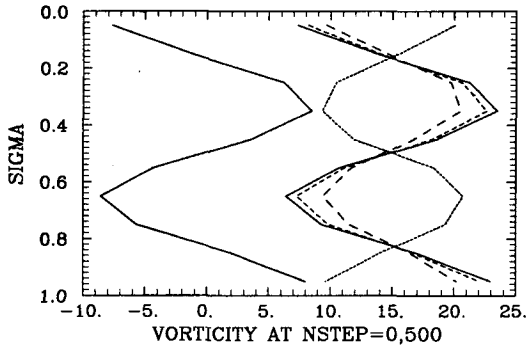

FIG. 2. As in Fig. 1 except for third internal gravity mode.

TABLE 1.

Model	M1	M2	M3
Type of vertical discretization	Finite element unstaggered	Finite element unstaggered	Finite difference staggered
Top boundary condition ($\dot{\sigma} = 0$) at:	$\sigma_1 = 0.01$	$\sigma_1 = 0.01$	$\sigma_0 = 0$
Helmholtz equation for:	$'P$	W	W

for W^+. The reason for using M2 is that the third model (M3), being a stripped-down version of the Canadian Meteorological Center's operational model, also solves a Helmholtz equation for W^+, although it does so by using a staggered second-order finite difference scheme in the vertical. Thus, M2 was used in order to isolate as much as possible the sole effect of using two different vertical discretization schemes.

Except for these differences, the three models are otherwise identical. They are all global, with a triangular spectral truncation at wave number 42; the vertical resolution is 15 equally spaced sigma levels extending from $\sigma_1 = 0.01$ at the top to $\sigma_N = 1.0$ at the ground for M1 and M2, and $\sigma_N = 0.99$ for M3. A $K\nabla^6$ horizontal diffusion term was added to the momentum and thermodynamic equations, along with a dry convective adjustment. Surface friction was also included (with a similar algorithm in all models, described in B83) in the form of a Cressman drag coefficient. The mountain field was taken from the ECMWF, and spectrally truncated at wavenumber 42, starting from a 216 × 108 latitude–longitude global grid.

Error statistics were obtained from an ensemble of seven 7-day global integrations. The initial time and verifying analyses were chosen from the FGGE-IIIb data set; five of the seven cases were picked from the ten interesting cases selected by the Working Group on Numerical Experimentation (WGNE). In Table 2 the starting dates for the seven series of integrations are given. Most of the results are presented in the form of a vertical average (over seven pressure levels extending from 1000 mb to 200 mb) of the root mean square error (rms) in the geopotential height with respect to the verifying analysis, at intervals of 24 hours from day 0 to day 7. In Figs. 3–6, the continuous line is the persistence rms error, while the thin and coarse

TABLE 2. Starting dates of the integrations.

0000 GMT 21 Dec 78
0000 GMT 02 Jan 79
1200 GMT 21 Jan 79
1200 GMT 12 Feb 79
1200 GMT 18 May 79
1200 GMT 04 Aug 79
1200 GMT 18 Sep 79

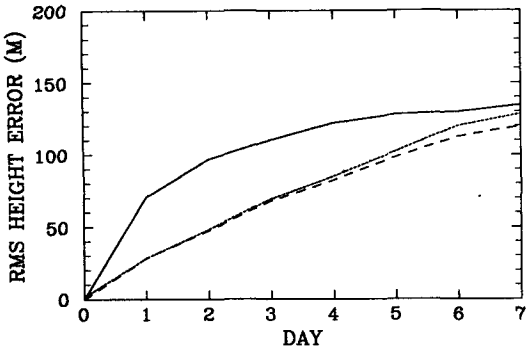

FIG. 3. Vertical average over seven pressure levels and over seven integrations of the root mean square error in geopotential height (in meters) as a function of integration time (in days). Full line is persistence, thin dashed line is finite-difference model (M3), coarse dashed line is old finite-element model (M2). Vertical resolution of 15 sigma levels.

dashed lines represent the M3 and M2 rms errors respectively.

Looking first at Fig. 3, it is observed that the finite-element integrations (M2) are at all times slightly better than the finite-difference integrations (M3). At the end of the integration period, M2 shows an increase in predictability of roughly one day. However, taking as a rough estimate of the climatological variance the maximum persistence error divided by the square root of two (95 m), we observe that, as both forecasts cross that value (between day 4 and day 5), the increase in predictability is roughly six hours for M2. We should mention at this point that this average behavior over seven cases was also observed in six of the seven cases, one case showing no significant difference between M2 and M3. Thus even though the sample is small we believe the results are significant and show that, at least for medium range forecasts, use of the finite element technique increases the accuracy of the forecast.

Now, when we first presented these results, the criticism was made that this difference could also be explained by the different responses of M2 and M3 to surface drag. We felt this criticism to be legitimate, and

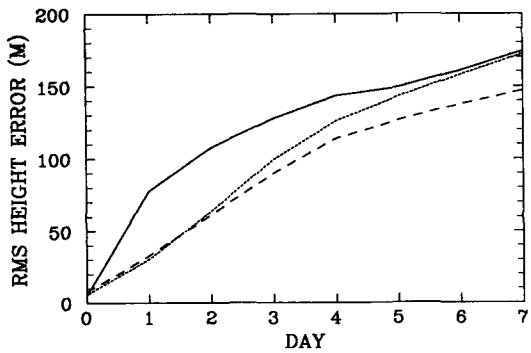

FIG. 4. As in Fig. 3 except for case of 1200 GMT 12 February 1979, and vertical resolution of 8 sigma levels.

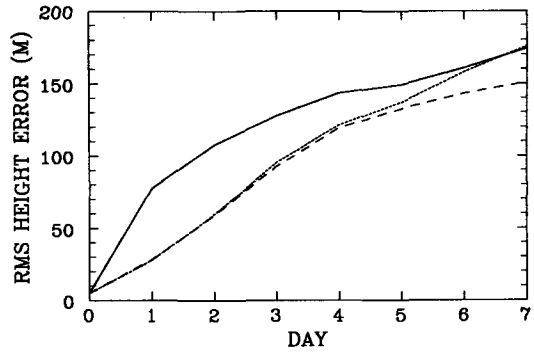

FIG. 5. As in Fig. 4 except for 15 sigma levels.

decided to perform another series of integrations in order to clear away any ambiguity. We integrated M2 and M3 with 8, 15 and 29 levels, thus effectively halving the vertical grid length every time. This was done for the 1200 GMT 12 February 1979 case. The results are displayed in Figs. 4–6. We observe the following: (i) As resolution is increased both models converge toward the same solution. (ii) The rate of convergence is faster for the finite-element model M2: with 8 sigma levels, M2 gives a more accurate solution after 2 days of integration; at 15 levels, this is true after 4 days, and at 29 levels, 5 days. (iii) M2 has essentially converged at 15 levels, as can be observed by comparing Figs. 5 and 6. This is not the case for M3, which still shows some improvement at 29 levels. From this we conclude that M2 is indeed more accurate than M3, irrespective of its response to the surface drag.

A corollary of these three experiments is that for a triangular 42 spectral truncation, the optimum vertical resolution is around 15 levels. A sizable gain is obtained by going from 8 to 15 levels, whereas going from 15 to 29 does not result in significant improvement.

The new formulation (M1) was also integrated on the seven cases and compared with the old finite-element formulation (M2). Apart from the difference in the formulation, there is also a small change in the surface drag; referring the reader to B83, a linear profile was used in M1, whereas a quadratic profile was used

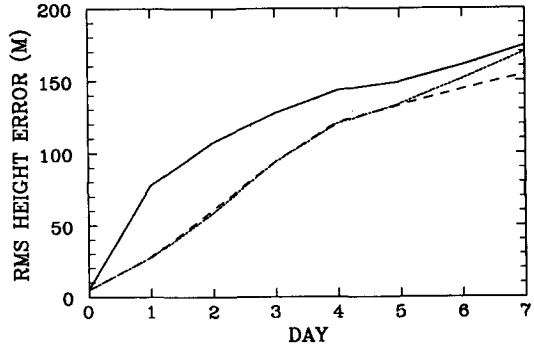

FIG. 6. As in Fig. 4 except for 29 sigma levels.

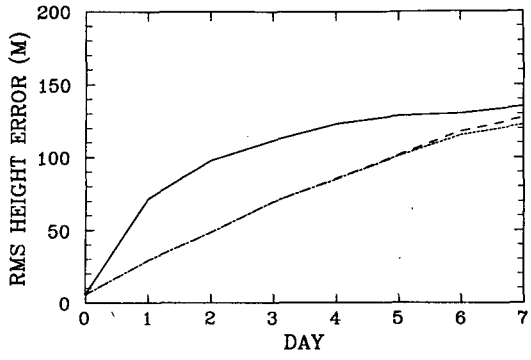

FIG. 7. As in Fig. 3 except thin dashed line is the old finite-element version and coarse dashed line is the new finite-element version.

in M2. The result is shown in Fig. 7. It is seen that both M1 and M2 yield similar results in terms of rms scores, a slight difference appearing at the end of the integration period, which we attribute to the different surface drag profile. This is not to say, however, that the actual flow configurations are identical: it was pointed out in the preceding subsection that the new formulation was free of vertical decoupling in the linear frictionless integrations, and it was hoped that this would still be the case in the fully nonlinear model, with friction included. In order to show this, we have taken two north–south cross sections of the meridional wind on the computational (horizontal and vertical) grid after a four day integration of two identical versions of M1 and M2 (i.e., same surface drag parameterization). The results are displayed in Figs. 8 and 9 for M1 and M2 respectively, and speak for themselves. The strong vertical decoupling that is present in the northern latitudes for M2 is completely absent in the M1 integration. Thus we may conclude that the new formulation has been successful in eliminating the "noise" problem present in the old formulation, without any loss in accuracy of the solution, or any *ad hoc* vertical diffusion term. Moreover, it turns out that the new scheme is 15% more efficient than the previous one, which is certainly an advantage in an operational context.

5. Conclusions

In this paper, we have described an (almost) adiabatic version of a global spectral model using a finite-element vertical discretization scheme. A series of linear integrations and global forecasts were performed in which this model was compared with another earlier finite element version and with a stripped-down version of the Canadian Meteorological Center's operational model, which uses staggered second-order finite differences in the vertical. In linear integrations, the finite-element model outperforms the finite-difference model, particularly in the formulation that uses a fourth-order scheme. In the global forecasts, the three models pro-

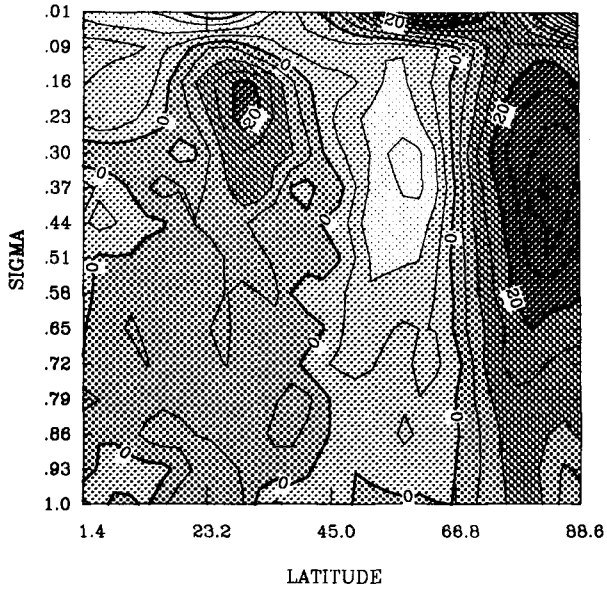

FIG. 8. North–south cross section (from equator to pole) on the Gaussian transform grid and at the model sigma levels of the meridional wind v in m s^{-1}, at day 4 of new finite-element version integration (M1) for 1200 GMT 12 February 1979 case. The cross section is taken at 90°W longitude. Pale shadings indicate negative (northerly) winds, darker shadings indicate positive (southerly) winds.

duce relatively similar results, with an increasing gain in predictability (as measured by an rms score) as the length of integration increases for the two finite-element versions. As the rms scores cross climatology (5 days) this gain is 6 hours, and it increases to 24 hours after 7 days of integration. A series of vertical resolution experiments seems to indicate that this gain can be attributed to the higher accuracy of the finite element

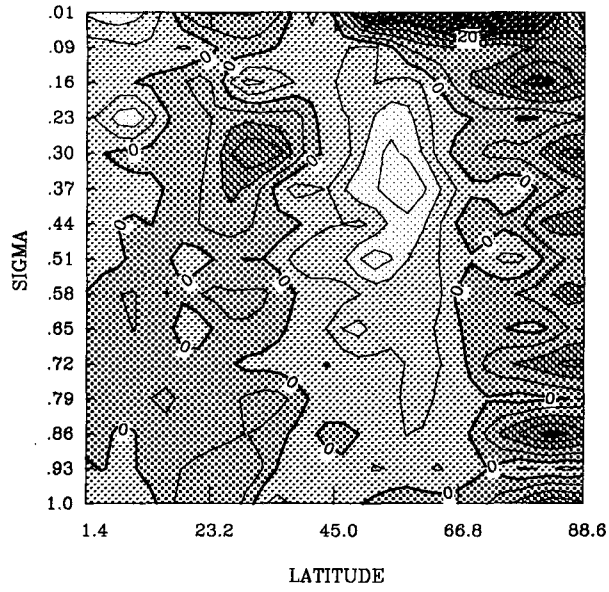

FIG. 9. As in Fig. 8 except for old finite-element version (M2).

schemes. Based on these results, work is now in progress to couple the model to a sophisticated finite-element boundary layer model, and to include additional physical parameterization terms. Preliminary experiments have indicated that this should lead to large gains in predictability for medium range forecasts.

Acknowledgments. The authors gratefully acknowledge the many stimulating discussions with their RPN colleagues, particularly Drs. André Robert, Andrew Staniforth, Jean Côté and Claude Girard. We also wish to thank Mr. Michel Valin and Mrs. Claudette Thibeault for their programming help, and Ms. Maryse Ferland for her patience and superb text editing of the successive drafts of this work.

APPENDIX A

Definition of the Projection and Second Derivative Operators

We repeat here for convenience the definition of the Chapeau function $\{e^i(\sigma),\ i = 1, N\}$, $\sigma_0 = \sigma_1$, $\sigma_{N+1} = \sigma_N$:

$$e^i(\sigma) = \begin{cases} 0 \quad \text{if} \quad \sigma < \sigma_{i-1} \quad \text{or} \quad \sigma > \sigma_{i+1} \\ \min\left\{\dfrac{\sigma - \sigma_{i-1}}{\Delta_{i-1}}, \dfrac{\sigma_{i+1} - \sigma}{\Delta_i}\right\}, \end{cases} \tag{A1}$$

where

$$\Delta_i = \sigma_{i+1} - \sigma_i. \tag{A2}$$

We let $\mathbf{P}$ note the projection operator in matrix form, with elements given by

$$\mathbf{P}_{ij} = \int_{\sigma_1}^{\sigma_N} e^i e^j d\sigma. \tag{A3}$$

Substituting (A1) and (A2) into (A3), we obtain

$$\mathbf{P}_{11} = \frac{1}{3}\Delta_1, \quad \mathbf{P}_{ii} = \frac{1}{3}(\Delta_{i-1} + \Delta_i), \quad \mathbf{P}_{NN} = \frac{1}{3}\Delta_{N-1}, \tag{A4}$$

$$\mathbf{P}_{i,i+1} = \mathbf{P}_{i+1,i} = \frac{\Delta_i}{6}, \tag{A5}$$

all other elements being zero. Thus $\mathbf{P}$ is a tridiagonal matrix. The second derivative operator (weighted by σ^β) is written $\mathbf{P}^\beta_{\sigma\sigma}$ in matrix form, its elements in turn given by

$$(\mathbf{P}^\beta_{\sigma\sigma})_{ij} = -\frac{1}{R\gamma_0}\int_{\sigma_1}^{\sigma_N} \sigma^\beta e_\sigma^i e_\sigma^j d\sigma, \quad 1 < j < N, \tag{A6}$$

$$(\mathbf{P}^\beta_{\sigma\sigma})_{i1} = -\langle\ \ \rangle_\sigma|_{\sigma_1} - \frac{1}{R\gamma_0}\int_{\sigma_1}^{\sigma_N} \sigma^\beta e_\sigma^i e_\sigma^j d\sigma, \quad j = 1, \tag{A7}$$

$$(\mathbf{P}^\beta_{\sigma\sigma})_{iN} = \langle\ \ \rangle_\sigma|_{\sigma_N} - \frac{1}{R\gamma_0}\int_{\sigma_1}^{\sigma_N} \sigma^\beta e_\sigma^i e_\sigma^j d\sigma, \quad j = N, \tag{A8}$$

where we have used (3.1) and (3.2) with $\beta = 1 - \alpha$. Substituting (A1) and (A2) into (A6) gives

$$(\mathbf{P}^\beta_{\sigma\sigma})_{ii} = -\frac{1}{R\gamma_0}\left(\frac{\delta_{i-1}}{\Delta_{i-1}^2} + \frac{\delta_i}{\Delta_i^2}\right), \tag{A9}$$

$$(\mathbf{P}^\beta_{\sigma\sigma})_{i,i+1} = (\mathbf{P}^\beta_{\sigma\sigma})_{i+1,i} = \frac{1}{R\gamma_0}\frac{\delta_i}{\Delta_i^2}, \tag{A10}$$

with

$$\delta_i = \begin{cases} \dfrac{1}{\beta+1}(\sigma_{i+1}^{\beta+1} - \sigma_i^{\beta+1}), & \beta \neq -1 \\ \ln\left(\dfrac{\sigma_{i+1}}{\sigma_i}\right), & \beta = -1. \end{cases} \tag{A11}$$

To compute the first term of the rhs of (A7) and (A8), we use (2.12), which relates the first derivative of P at either $\sigma = \sigma_N = 1$ or $\sigma = \sigma_1$ to its value at the surface P_N [written P_s in (2.12)]. Thus, in (A7), we get a nonzero contribution to $(\mathbf{P}^\beta_{\sigma\sigma})_{N1}$ from this term, e.g.

$$(\mathbf{P}^\beta_{\sigma\sigma})_{N1} = \frac{\sigma_1}{RT_s^*}. \tag{A12}$$

The other contribution comes from the integral and gives

$$(\mathbf{P}^\beta_{\sigma\sigma})_{11} = -\frac{1}{R\gamma_0}\frac{\delta_1}{\Delta_1^2}. \tag{A13}$$

In (A8), both the first and the second term contribute to $(\mathbf{P}^\beta_{\sigma\sigma})_{NN}$ giving

$$(\mathbf{P}^\beta_{\sigma\sigma})_{NN} = -\frac{1}{R\gamma_0}\left(\frac{\delta_{N-1}}{\Delta_{N-1}^2} + \frac{\gamma_0}{T_s^*}\right). \tag{A14}$$

As mentioned in the derivation of (3.4), we get an exact cancellation of the rhs of (2.12) when the operator is applied to P^- in (3.7). Thus, $\mathbf{P}^\beta_{\sigma\sigma}$ is quasi-tridiagonal, since there is an "extra" nonzero element in the upper right corner of the matrix. Gaussian elimination can still be used effectively, and since all the elements are constant in time, the elimination step can be performed once and for all at the beginning of the forecast, and the results stored in three vectors of length N for each eigenvalue of the horizontal Laplacian operator. This allows a very efficient solution of the Helmholtz equation for P^+ in spectral space.

APPENDIX B

Variable Step Multistep Method

In this appendix we present a "variable step multistep method" to solve the equations

$$\frac{d^r y}{dx^r} = f, \quad r = 1, 2, \tag{B1}$$

on a possibly irregular mesh $\{x_i, i = 1, N\}$, when f is at most linear in y. For simplicity we shall assume f to be independent of y; the extension is rather simple.

The method presented here is for the solution of linear equations and is devised to yield the greatest possible accuracy for the nodal values on an irregular mesh while remaining of the same complexity as the finite-element method. Both types of algorithms can be mixed in a model, the finite-element Galerkin procedure handling of the nonlinear terms controlling the aliasing.

The present method consists of a second-order difference equation to represent (B1) in the interior points and suitable finite-difference formulae at the boundaries.

For the interior points $1 < i < N$, we write

$$\frac{y_{i+1} - y_i}{h_i}(-1)^{r+1}d\frac{(y_i - y_{i-1})}{h_{i-1}} = af_{i-1} + bf_i + cf_{i+1}, \tag{B2}$$

where $h_i = x_{i+1} - x_i$ and the as yet unspecified coefficients a, b, c and d depend on r and i. The meaning of (B2) is quite evident: In the first-order case the derivative at the point i is approximated as an average of the slopes estimated on both sides of the node while the right-hand side is averaged over the three mesh points; in the second-order case we take a difference of the slopes to get an estimate of the second derivative. We restrict ourselves in (B2) to a second-order recursion relation because it leads eventually to tridiagonal or quasi-tridiagonal matrix problems as in the finite-element method.

The coefficients are determined by requiring the algorithm to be exact for $y = (x - x_i)^m$, $m = 1, 4$ in the interval x_{i-1}, x_{i+1}. Note that it is exact for $y =$ constant. The corresponding f are

$$f = \frac{d^r}{dx^r}(x - x_i)^m, \tag{B3}$$

and there results the set of linear equations

$$h_i^{m-1} + (-1)^{m-r}h_{i-1}^{m-1}d = \frac{m!}{(m-r)!}[(-1)^{m-r}h_{i-1}^{m-r}a + \delta_{m,r}b + h_{i+1}^{m-r}c], \tag{B4}$$

where $\delta_{m,r}$ is the Kronecker delta.

The solution for the first-order equation ($r = 1$) is given by

$$a = \frac{1+\epsilon}{2(2+\epsilon)\epsilon^2}, \quad b = (1+\epsilon)^2 a,$$
$$c = \epsilon^2 a, \quad d = \frac{1+2\epsilon}{(2+\epsilon)\epsilon^2}, \tag{B5}$$

with $\epsilon = h_{i-1}/h_i$. If the mesh is uniform one gets the usual finite-element or Simpson's weights. The solution for the second-order equation ($r = 2$) is given by

$$a = \frac{h_i}{12}\left[1 + \frac{h_{i-1}^2 - h_i^2}{h_{i-1}h_i}\right],$$
$$b = \frac{h_{i-1} + h_i}{12}\left[5 + \frac{(h_{i-1} - h_i)^2}{h_{i-1}h_i}\right],$$
$$c = \frac{h_{i-1}}{12}\left[1 + \frac{h_i^2 - h_{i-1}^2}{h_{i-1}h_i}\right], \quad d = 1. \tag{B6}$$

If the mesh is uniform one gets the so-called "fourth-order finite-element" or Numerov's weights. By construction, the truncation error on y is $O(h^5)$ and on a uniform grid the symmetry conspires to reduce the error to $O(h^6)$ for the second-order equation (superconvergence).

We now look at the boundary. Let us first consider the first order equation. We can write

$$\frac{y_2 - y_1}{h_1} = \sum_{m=1}^{s} W_m f_m \tag{B7}$$

and require that it be exact for $y = (x - x_1)^m$, $m = 1, s$.

If the problem at hand consists in solving for y with the value y_1 given then (B2) and (B7) will give the result in only one pass.

The choice $s = 2$ gives $W_1 = W_2 = 1/2$ (the trapezoidal rule) and a tridiagonal right-hand side matrix; but the accuracy is reduced to $O(h^3)$. Furthermore this larger error propagates upward as the substitution is done; on a uniform mesh it affects only the even points. The amplitude of this computational mode can be reduced if s is taken greater than 2 at the expense of a small increase in the computational effort. This is the strategy that we have adopted. For $s = 3$ the weights are

$$W_1 = \frac{3\epsilon - 1}{6\epsilon}, \quad W_2 = \frac{3\epsilon - 2}{6(\epsilon - 1)}, \quad W_3 = \frac{-1}{6\epsilon(\epsilon - 1)}, \tag{B8}$$

with

$$\epsilon = \frac{x_3 - x_1}{x_2 - x_1}.$$

The corresponding formulae for the other boundary are readily obtained.

In the case of the second-order equation, the treatment depends on the type of boundary conditions. If they are of the essential type, i.e. y_1 and y_N specified, then (B2) is sufficient. If on the other hand, the slopes are prescribed (p_1 and p_N at x_1 and x_N respectively) we write

$$\frac{y_2 - y_1}{h_1} - p_1 = \sum_{m=1}^{s} W_m f_m \tag{B9}$$

and a similar relation at the other boundary. Again the weights are chosen such that the relation is exact for $y = (x - x_1)^m$, $m = 2, s + 1$ ($m = 1$ is trivially exact). For the tridiagonal algorithm ($s = 2$) the solution is

$$W_1 = \frac{h_1}{3}, \quad W_2 = \frac{h_i}{6} \tag{B10}$$

and the error is $O(h^4)$.

We will not dwell on the stability and convergence of the algorithm presented here. It is worth mentioning however that the right-hand side (averaging) matrix of the recursion relation is diagonally dominant ($b > a + c$).

REFERENCES

Beaudoin, C., and A. Staniforth, 1980: Experiments with a model using the finite element method for vertical discretization. *Research Activities in Atmospheric and Oceanic Modelling,* I. D. Rutherford, Ed., GARP, WGNE, Rep. No. 21, 108 pp.

Béland, M., J. Côté and A. N. Staniforth, 1982: A Finite element formulation of the vertical discretization. *Research Activities in Atmospheric and Oceanic Modelling,* I. D. Rutherford, Ed., GARP, WCRP, Rep. No. 3, 144 pp.

——, —— and ——, 1983: The accuracy of a finite-element vertical discretization scheme for primitive equation models: Comparison with a finite-difference scheme. *Mon. Wea. Rev.,* **111,** 2298–2318.

Côté, J., M. Béland and A. N. Staniforth, 1983: Stability of vertical discretization schemes for semi-implicit primitive equation models: Theory and application. *Mon. Wea. Rev.,* **111,** 1189–1207.

Daley, R., C. Girard, J. Henderson and I. Simmonds, 1976: Short-term forecasting with a multi-level spectral primitive equations model. *Atmosphere,* **14,** 98–134.

Robert, A. J., J. Henderson and C. Turnbull, 1972: An implicit time integration scheme for baroclinic models of the atmosphere. *Mon. Wea. Rev.,* **100,** 329–335.

Staniforth, A. N., and R. W. Daley, 1977: A finite element formulation for the vertical discretization of sigma coordinate primitive equation models. *Mon. Wea. Rev.,* **105,** 1108–1118.